

Hybrid neural denoising for resource-efficient near- and sub-threshold radio triggering of extensive air showers

Alperen Aksoy^a, Ilja Bekman^a, Markus Cristinziani^b, Eric-Teunis de Boone^b, Vesselin Dimitrov^{a,b}, Qader Dorosti^{b,1}, Chimezie Eguzo^a, Stefan Heidbrink^c, Stefan van Waasen^{a,d}, Andre Zambanini^a

^a*Peter Grünberg Institute – Integrated Computing Architectures (ICA | PGI-4), Forschungszentrum Jülich GmbH, Germany*

^b*Center for Particle Physics Siegen, Department Physik, Universität Siegen, Germany*

^c*Elektronikentwicklungslabor, Department Physik, Universität Siegen, Germany*

^d*Faculty of Engineering, Communication Systems, University of Duisburg-Essen, Germany*

E-mail: dorosti@hep.physik.uni-siegen.de

¹Corresponding author.

ABSTRACT: Autonomous radio self-triggering for extensive air showers must reject variable radio-frequency interference while preserving sensitivity to weak pulses and remaining compatible with station-level edge hardware. This work presents a hybrid neural trigger in which waveform recovery and signal classification are treated as a single deployment-constrained problem. A compact convolutional denoiser first maps a noisy single-channel trace to a cleaned estimate of the air-shower pulse; a compact classifier then evaluates the cleaned waveform. The method is tested with measured high-interference background traces and detector-folded air-shower pulses produced with the Pierre Auger *Offline* simulation chain. The signal construction deliberately populates the near- and sub-threshold regime, where autonomous radio triggering is most limited. Model selection and deployment are linked from the outset through hyperparameter optimisation, quantisation-aware training, high-granularity fixed-point quantisation, hls4m1 firmware export, high-level synthesis, and register-transfer-level validation. The study therefore tests not only whether a neural decision stage can classify traces, but also whether an explicit waveform-denoising stage provides a useful trigger representation that can be realised in field-programmable gate array hardware. The denoiser alone turns a simple peak-envelope decision into an efficient weak-pulse trigger, showing that the cleaned waveform carries trigger-relevant information beyond a final classifier score. In the full denoiser–classifier chain, the hybrid trigger improves the overall signal-background separation and the efficiency at fixed false-positive rates: at a false-positive rate of 10^{-4} , it retains about 41% of the held-out signal traces in the deliberately weak-signal benchmark, while the classical peak-envelope trigger retains none. Since weak station-level pulses are the limiting signature for inclined and otherwise radio-faint air showers, this gain reduces a trigger-level bias against the event classes for which radio detection is most valuable. The cleaned waveform also preserves timing and peak-amplitude structure sufficiently for station-level diagnostics, feature extraction, and selective readout. The implemented firmware meets timing on representative field-programmable gate array targets with microsecond-scale latency and compact arithmetic-resource demand. These results establish hybrid neural denoising as a practical route toward radio-only triggering for weak and inclined air-shower signals in noisy environments.

KEYWORDS: Performance of High Energy Physics Detectors, Large detector systems for particle and astroparticle physics, Detector modelling and simulations II, Digital signal processing, Trigger concepts and systems, Pattern recognition

Contents

1	Introduction	1
2	Data sets and signal construction	3
2.1	Measured noise data	3
2.2	Detector-aware signal simulation with the Pierre Auger <i>Offline</i> framework	3
2.3	Signal injection and amplitude scaling	4
2.4	Training, validation, and test samples	5
3	Hybrid trigger method	7
3.1	Trigger concept and processing chain	7
3.2	Denoiser and classifier model families	7
3.3	Hyperparameter optimisation setup and objective	9
3.4	Quantisation-aware training and high-granularity quantisation	11
4	Trigger performance	13
4.1	Evaluation metrics and operating points	13
4.2	Classical threshold baseline	13
4.3	Comparison of trigger branches	14
5	FPGA implementation	18
5.1	Target platforms and tool flow	18
5.2	Resource use, timing, and power	19
5.3	Hardware-cost reduction relative to the published FPGA study	19
5.4	End-to-end RTL validation	20
6	Discussion	22
6.1	Physics and operational implications	22
6.2	What the denoiser adds beyond a decision-level trigger	23
6.3	Limitations and robustness checks	27
7	Summary and outlook	28

1 Introduction

Ultra-high-energy cosmic rays (UHECRs) are studied with large ground-based observatories that combine particle detectors, fluorescence telescopes, and radio antennas [1–3]. Radio detection has become particularly attractive because it offers a cost-effective technique with high duty cycle, broad sky coverage, and sensitivity to the electromagnetic component of extensive air showers (EAS) [4].

By exploiting the geomagnetic and charge-excess emission mechanisms [5, 6], radio arrays can reconstruct shower properties such as the primary energy and the depth of shower maximum with competitive precision [7, 8].

One of the strongest motivations for radio-only triggering is the detection of inclined air showers. In that regime, the particle component is strongly attenuated before reaching ground level, whereas the radio pulse can still remain measurable over large footprints [8]. Existing radio arrays therefore benefit from radio sensitivity precisely in the part of phase space where external particle-detector triggers become least efficient. A reliable self-trigger is consequently a key ingredient for extending the science reach of future cosmic-ray and neutrino observatories.

The long-standing obstacle is the radio background itself. In realistic field conditions, transient anthropogenic interference and narrow-band radio-frequency interference (RFI) generate large numbers of signal-like excursions that simple threshold triggers cannot reject efficiently [9–11]. A practical radio self-trigger must therefore do more than separate signal from background in principle: it must improve near-threshold selection while operating at MHz-scale trial rates and still fit into the latency and resource budget of station-class field programmable gate array (FPGA) hardware.

A recent study by our group demonstrated a proof-of-principle classifier-only trigger trained on measured high-interference noise and simulated air-shower pulses, and showed that it outperforms a classical threshold trigger while preserving its performance after fixed-point conversion and FPGA-oriented synthesis [12]. That result established the feasibility of AI-based radio self-triggering in a realistic RFI environment, but it also left two natural next questions. First, can the trigger sensitivity be improved further, especially in the near- and sub-threshold regime where weak pulses are most difficult to recover? Second, can the model-development strategy be changed such that the final implementation becomes substantially cheaper on the FPGA targets that matter for autonomous station-level deployment?

The present work addresses both questions by moving from a classifier-only trigger to a hybrid denoiser-plus-classifier pipeline and by making hardware constraints part of the model-development loop from the outset. The denoiser is introduced to recover weak pulses before the trigger decision, while hyperparameter optimisation (HPO), quantisation-aware training (QAT), and high-granularity quantisation (HGQ) [13] are used to search for models that retain trigger performance at drastically reduced implementation cost. At the same time, the signal construction is made more realistic by replacing the earlier proof-of-principle simulation workflow with a detector-aware chain based on the Pierre Auger *Offline* software framework [14], while reusing the same measured-noise dataset as in the published study.

The remainder of this paper is organised around these three developments. We first define the measured-noise benchmark, the detector-aware signal simulation, and the near-threshold signal construction used for the trigger study. We then introduce the denoiser–classifier architecture, the hyperparameter-optimisation procedure, and the QAT/HGQ workflow used to obtain firmware-compatible models. The trigger-performance analysis compares the denoiser-assisted branches with a classical peak-envelope threshold baseline under common fixed-false-positive operating conditions. The hardware study then evaluates the post-implementation resource and power demand of the resulting firmware and compares it with the previously published classifier-only FPGA implementation. Together, these studies quantify both the near-threshold trigger gain of the hybrid

pipeline and the reduction in FPGA deployment cost achieved by the hardware-aware model-development workflow.

2 Data sets and signal construction

This section defines the measured background data, the detector-aware signal simulation, and the construction of the datasets used for the trigger study. The measured-noise traces and basic trace-conditioning convention follow the same experimental setup used previously, while the signal side is rebuilt around a detector-aware air-shower simulation based on the Pierre Auger *Offline* framework [14].

2.1 Measured noise data

We use the measured background dataset described in Ref. [12]. The noise traces were recorded on the physics campus of the University of Siegen with a butterfly antenna, a 30 dB low-noise amplifier, and a digital oscilloscope. The traces are digitally restricted to the 30 MHz to 80 MHz band and represented at a sampling rate of 250 MHz, consistent with the timing scale relevant for radio detection of extensive air showers.

The measured background corresponds to a difficult high-interference environment with both transient disturbances and prominent narrow-band RFI components. Keeping this background pool unchanged preserves a common and deliberately challenging reference point for the threshold trigger, the classifier-only branch, and the denoiser–classifier pipeline. Full details of the acquisition setup, the duration of the measurement campaign, and the observed RFI features are not repeated here.

2.2 Detector-aware signal simulation with the Pierre Auger *Offline* framework

The signal model is based on a set of CoREAS/CORSIKA air-shower simulations produced within the Pierre Auger Collaboration for energy-scale studies with the Auger Engineering Radio Array (AERA) [15]; the showers were generated event by event following Ref. [16]. The parent production is based on 844 high-quality AERA air showers with reconstructed SD energies above 3×10^{17} eV; for each event, one proton and one iron shower are simulated with CoREAS/CORSIKA, using the measured shower geometry and calorimetric-energy estimate of the corresponding event. The production described in Ref. [16] uses Sibyll 2.3d and UrQMD as interaction models together with per-event atmospheric profiles derived from GDAS.

The Pierre Auger *Offline* chain provides a validated detector simulation including the antenna response and the subsequent electronic signal chain. In particular, the detector model used here includes the response of the AERA butterfly antennas together with the associated low-noise-amplifier electronics, so that the simulated detector output is matched to an experimentally calibrated radio-detector configuration. For the present work, we use the detector-folded voltage traces from this simulation chain as the starting point for signal injection. To match the acquisition system used for the measured-noise dataset of Sec. 2.1, we retain only the low-gain signal chain, discard the additional amplification stage used in the AERA high-gain branch, and adapt the simulated traces to the 250 MHz sampling used throughout this study.

The resulting library spans a broad range of shower geometries and pulse morphologies, inherited from the event-by-event AERA production and therefore covering variations in zenith angle, azimuth, X_{\max} , and antenna–core distance. After the detector folding and adaptation to the local readout convention, we retain only traces in which the pulse reaches at least 50 ADC counts relative to the corresponding zero-crossing reference. This requirement suppresses effectively empty detector responses while keeping the signal library focused on traces that contain a resolved pulse candidate; lowering the retention value to 25 ADC counts was checked and did not materially change the benchmark conclusions. After the low-gain selection and the nominal 50-ADC requirement, 9318 detector-folded traces remain in the retained signal library.

Combined with the measured background dataset of Sec. 2.1, this construction yields signal-containing traces in which realistic detector-folded pulses are embedded into experimentally measured radio noise.

2.3 Signal injection and amplitude scaling

The detector-level pulses produced with the Pierre Auger *Offline* chain are injected into measured noise traces at random temporal positions, using the same measured-noise pool described above. The injection positions include an edge margin before the final trace trimming, so the pulse maximum is not deliberately centred on the boundary of the 128-sample analysis frame. Residual fixed-window effects from finite pulse width, filtering, and trimming are nevertheless retained in the reported efficiencies; in a streaming deployment, overlapping or sliding trigger windows could reduce such boundary losses, with the operating threshold retuned for the corresponding change in background trial rate. This preserves the real transient and narrow-band interference structure of the recorded background while allowing controlled construction of signal-containing traces. Unless noted otherwise, noise-only and signal-containing traces are passed through the same digital conditioning chain, so that the trigger models never see differently processed background and signal samples.

In addition to the natural amplitude variation already present in the simulated event library, we apply a controlled post-simulation amplitude scaling in order to scan the near-threshold and sub-threshold regime with sufficient granularity. This scaling is not introduced as a replacement for the detector simulation, but as a practical way to probe trigger efficiency across a dense signal-strength range while keeping the detector-aware pulse shapes fixed. In that sense, the scaling step should be interpreted as part of the trigger-characterisation procedure rather than as an attempt to redefine the physical event distribution. The signal-containing samples used in the present study are intentionally concentrated more strongly in the weak-signal regime, because the central question is whether the denoiser–classifier pipeline improves performance close to and below the effective trigger threshold. Since this construction deliberately changes the signal-strength mixture, sample-integrated quantities such as the receiver-operating-characteristic (ROC) area under the curve (AUC) are benchmark-dependent. The main performance interpretation is therefore based on fixed-FPR efficiencies and on their dependence on the signal-strength proxy, with an alternative global-scale signal construction used later as a robustness check of the amplitude-scaling procedure.

To characterise signal strength across the constructed datasets, we use a revised analysis-side signal-to-noise ratio (SNR) proxy for the histogram shown in figure 1. Let \mathcal{P} denote the pulse window localised from the Hilbert envelope of the paired pure `signal` trace around its main peak.

For a trace x , we then define

$$\text{SNR}(x) = \frac{1}{\sigma_{\text{noise}}^2} \left(\frac{1}{|\mathcal{P}|} \sum_{i \in \mathcal{P}} |\mathcal{H}(x)_i|^2 \right), \quad (2.1)$$

where $\mathcal{H}(x)$ denotes the Hilbert-envelope amplitude and σ_{noise}^2 is the variance of the paired background trace. For the signal distribution, x is the `signal` trace itself, so the plotted signal power is evaluated on the noisy waveform inside the pulse window. For the background distribution, the same pulse window is evaluated on the paired background trace. This differs from Ref. [12], where the signal-side quantity was based on the clean-pulse peak amplitude and the background-side quantity was localised directly from the noise trace itself. The revised proxy used here therefore tracks how strongly the pulse remains expressed inside the noisy waveform and provides a more direct signal-background comparison inside a common window. Qualitatively, the present benchmark should accordingly be read as more challenging at a given nominal SNR level than the benchmark of Ref. [12], since the earlier definition was tied to the clean pulse rather than to its noisy realisation. The resulting $\log_{10}(\text{SNR})$ distributions are shown in figure 1. They are intended to characterise the present benchmark and to show that it is populated much more strongly in the weak-signal regime, rather than to provide a one-to-one numerical comparison with the earlier histogram.

2.4 Training, validation, and test samples

Throughout the paper, the class `background` denotes measured noise-only traces, `pure signal` denotes detector-level simulated pulses without added noise, and `signal` denotes traces obtained by injecting a `pure signal` pulse into `background`. With this notation fixed, the denoiser is trained with `signal` traces as input and the corresponding `pure signal` traces as target, whereas the classifier is trained on `background` and `signal` traces. Hyperparameter optimisation is monitored on the **Cross-Validation Dataset**. For model development, the signal distribution is intentionally reweighted toward the near- and sub-threshold regime, while the noise distribution is kept unchanged.

The split is performed at the constructed-trace level. A constructed `signal` sample is defined by the detector-folded pulse, the measured background trace into which it is injected, the injection time, and the applied amplitude scale. Consequently, training and validation samples are disjoint as time-series traces, but they are drawn from the same parent library of detector-folded AERA simulations and from the same measured-noise campaign. The validation therefore tests generalisation to unseen pulse-noise realisations and amplitude scalings within this benchmark, rather than to a statistically independent shower-simulation production.

For the final physics and hardware comparisons, all methods are evaluated on held-out samples that are not used during model selection. **Validation Dataset 1** is the main signal-plus-background benchmark, and **Validation Dataset 2** is the large background-only sample used for false-positive studies. The same held-out samples are used throughout the ablation study of Sec. 4.3, so that the comparison remains one of trigger methods rather than of datasets.

Table 1 summarises the dataset definition used in the present study. The listed sizes correspond to the fixed split used throughout the analysis.

Table 1: Dataset definition used in the present study. The listed sample sizes and class compositions correspond to the fixed split used throughout the analysis.

Dataset	Current use in this work	Traces	Composition
Training Dataset	Full model training	150 000	50 000 background, 50 000 pure signal, 50 000 signal
Training Dataset	HPO training	15 000	denoiser: 7500 pure signal, 7500 signal; classifier: 7500 background, 7500 signal
Training Dataset	HPO cross-validation	10 000	denoiser: 5000 pure signal, 5000 signal; classifier: 5000 background, 5000 signal
Validation Dataset 1	Full model validation	150 000	50 000 background, 50 000 pure signal, 50 000 signal
Validation Dataset 2	False-positive estimate	1 000 000	background only

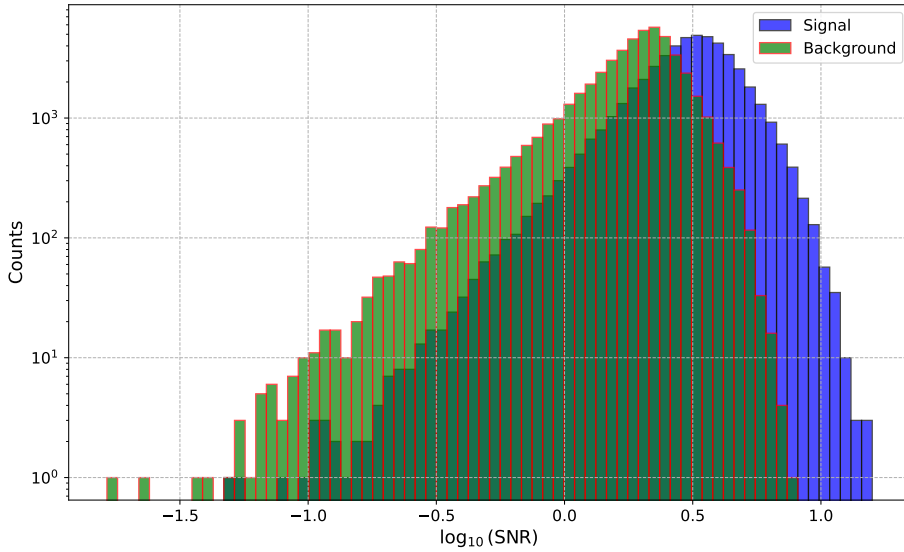


Figure 1: Distribution of $\log_{10}(\text{SNR})$ for the signal and background samples used in the present study, computed with the proxy defined in Eq. 2.1. The figure is intended to show that the benchmark is concentrated strongly in the weak-signal regime relevant for the denoiser-assisted trigger.

3 Hybrid trigger method

The present work moves from the classifier-only trigger of Ref. [12] to a deliberately co-designed pipeline in which waveform denoising, binary classification, and fixed-point deployment are treated as parts of a single trigger-development workflow. The underlying hypothesis is that weak air-shower pulses can be recovered more effectively if the trigger is allowed to perform a lightweight waveform-level cleaning step before the final signal-versus-background decision. At the same time, the model-development strategy is constrained from the outset by deployment requirements, so that improvements in trigger sensitivity are not obtained at the cost of impractical FPGA resource usage.

3.1 Trigger concept and processing chain

The trigger concept is a two-stage neural path operating on single-channel radio traces of length 128 samples. Let $\mathbf{x} \in \mathbb{R}^{128}$ denote one input trace. In the hybrid path, a denoiser f_θ first maps the noisy input waveform to a cleaned estimate,

$$\hat{\mathbf{x}} = f_\theta(\mathbf{x}), \tag{3.1}$$

and a classifier g_ϕ then maps either the denoised trace $\hat{\mathbf{x}}$ or, in the classifier-only reference case, the raw input \mathbf{x} to a signal probability

$$p_{\text{sig}} = g_\phi(\hat{\mathbf{x}}) \quad \text{or} \quad p_{\text{sig}} = g_\phi(\mathbf{x}). \tag{3.2}$$

A trigger is issued when p_{sig} exceeds an operating threshold τ . This decomposition makes it possible to test directly whether a waveform-level denoising step adds value beyond what can already be achieved by a compact decision-level classifier. Related convolutional-network studies have used this waveform-level perspective for radio-pulse identification and denoising in offline air-shower analyses [17, 18]; here, the same distinction between waveform recovery and decision making is used as a trigger-design question under fixed-point FPGA constraints.

The neural trigger path is compared primarily against a classical peak-envelope threshold trigger, which serves as the main non-neural baseline. This trigger operates on the peak amplitude of a signal-strength proxy and provides a conventional benchmark against which the gain of the denoiser-classifier pipeline can be evaluated. The previously published classifier-only model of Ref. [12] provides historical context for the development from a classifier-only trigger toward the denoiser-assisted hybrid pipeline.

From an implementation point of view, the full workflow proceeds from model development in Keras through quantisation-aware training and fixed-point export to firmware generation with hls4ml [19–21], followed by high-level synthesis and hardware-oriented validation. Figure 2 shows the workflow as a block diagram.

3.2 Denoiser and classifier model families

The architecture is not presented as a single hand-designed network. Instead, the method begins from two compact model families, one for denoising and one for classification, which are intentionally restricted to low-complexity 1D convolutional forms suitable for later FPGA deployment.

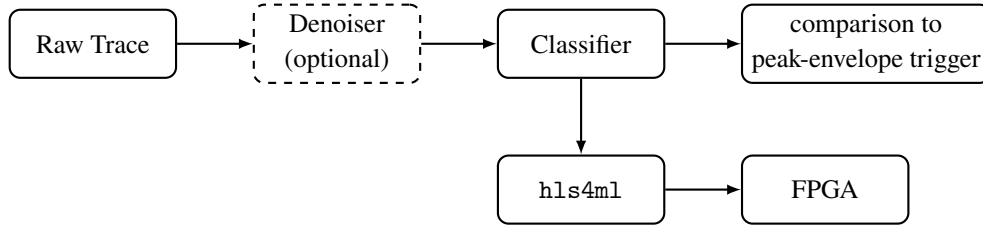


Figure 2: Compact overview of the processing chain: raw trace input, optional denoiser, classifier, followed by a comparison to a threshold based peak-envelope trigger and the quantisation and hardware deployment workflow (h1s4m1 \rightarrow FPGA).

Table 2: Training configuration for the denoiser and classifier models.

Training Component	Denoiser	Classifier
Loss function	Mean squared error	Binary cross-entropy
Optimiser	Adam	Adam
Learning-rate	0.0016	0.0011
Batch size	8	64
Stopping criterion	Early stopping (patience = 50)	Early stopping (patience = 20)

The classifier family consists of shallow 1D convolutional networks that alternate convolution, non-linearity, and pooling before a low-dimensional decision head. The selected classifier is a compact six-block Conv1D network with ReLU activations and MaxPool stages, followed by global average pooling and a final dense output node. This model performs binary discrimination between signal and background traces and currently contains 460 trainable parameters.

The denoiser family is formulated as a lightweight fully convolutional regression model that maps a noisy trace to a cleaned waveform estimate. The selected denoiser uses four Conv1D+ReLU blocks together with an additive residual path, two intermediate Conv1D+ReLU layers, a further convolutional refinement stage, and a final single-filter output projection followed by reshaping back to a one-dimensional trace. This model currently contains 868 trainable parameters.

Using the notation fixed in Sec. 2.4, the denoiser is trained as a waveform-regression model with signal traces as input and the corresponding pure signal traces as target, using a mean-squared-error loss. The classifier is trained with binary cross-entropy to distinguish signal from background. This notation is retained throughout the paper, so that the architectural description, the ablation study, and the hardware results all refer to the same sample definitions. Table 2 shows the key training parameters used for both models.

The input traces are normalised for training using z-score normalisation. For each raw sample value x_{raw} , the normalised value x is defined as

$$x = \frac{x_{\text{raw}} - \mu}{\sigma}, \quad (3.3)$$

where μ and σ denote the mean and standard deviation of the corresponding raw trace.

Figures 3 and 4 illustrate the denoiser response for representative background and signal traces. For the noise-only background case, where no physical pulse is present, the desired output is close to zero amplitude, whereas for the signal case the denoiser is expected to suppress noise while retaining the injected pulse structure.

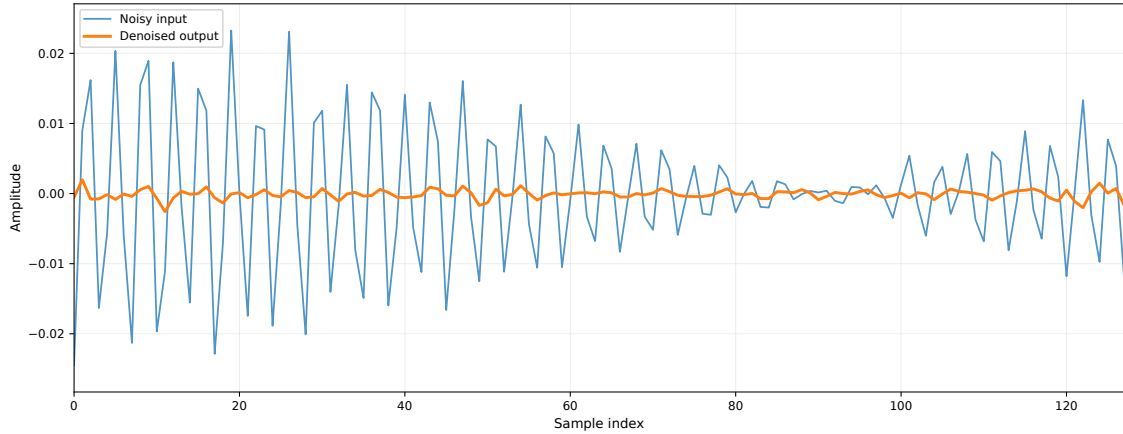


Figure 3: A denoised background (pure noise) trace. The blue curve shows the raw input trace, and the orange curve shows the denoised output. Since a background trace contains no simulated air-shower pulse, the target output is zero amplitude; the example illustrates that the denoiser suppresses the noise-only input without producing a signal-like pulse.

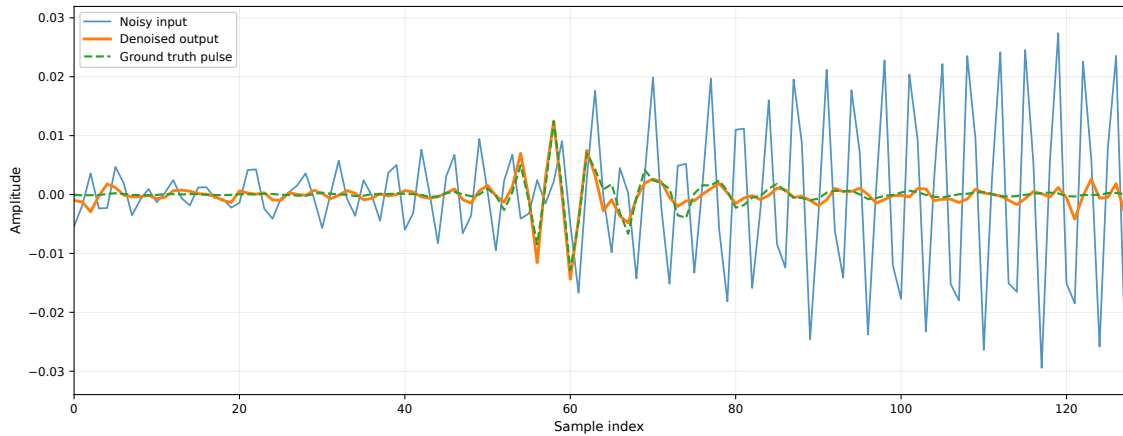


Figure 4: An example of a denoised signal trace. It can be seen that the signal is properly denoised with successful suppression of noise.

3.3 Hyperparameter optimisation setup and objective

Because even compact 1D convolutional models admit many architectural and training choices, model selection is automated with hyperparameter optimisation rather than fixed by manual trial

Table 3: HyperBand configuration used for model hyperparameter optimisation.

HyperBand Parameter	Denoiser	Classifier
Maximum training budget	60 epochs	50 epochs
Reduction factor	4	3
Objective	minimise validation loss	
Iterations	2	1
Number of brackets	3	4
Initial HPO candidates per bracket	3, 6, 16	4, 6, 12, 27

and error. The current optimisation strategy is based on HyperBand [22], which combines aggressive early stopping with successive halving. The basic logic is to train many candidate configurations for a small budget, rank them after partial training, discard the least promising ones, and reallocate the available budget to the surviving candidates. In this way, a comparatively large search space can be explored without fully training every candidate model.

For the trigger problem considered here, the natural search variables include the numbers of convolutional blocks, channel widths, kernel sizes, pooling pattern, residual connections or normalisation options, and training hyperparameters such as learning rate and batch size. The key methodological point is that model quality cannot be judged by classification accuracy alone. The search objective must also encode deployment realism, because a model that slightly improves the trigger metric while greatly increasing latency or digital signal processor (DSP) usage is not attractive for a station-class implementation.

Table 3 shows the HyperBand parameters used for the denoiser and classifier searches. The models have been optimised independently of each other. To make sure that HyperBand does not select models that are too costly for hardware deployment, the validation objective is constrained by model size. For the classifier, the validation binary cross-entropy (BCE) is augmented by a parameter-count penalty,

$$\mathcal{L}_{\text{clf}} = \text{BCE}(y, \hat{y}) + 0.55 \frac{N_{\text{par}}}{2000}, \quad (3.4)$$

where N_{par} is the number of trainable parameters. The denominator 2000 sets a reference scale for compact classifier candidates and makes the parameter term dimensionless. With this choice, a 2000-parameter model receives a loss penalty of 0.55, while the selected 460-parameter classifier receives a penalty of 0.13. The coefficient was chosen as an empirical compactness prior for the HyperBand ranking, so that larger models are accepted only if their validation loss improves enough to compensate for the additional parameters.

For the denoiser, the search uses a hard model-size constraint rather than a soft penalty. Candidate architectures above the sub-1000-parameter target are assigned a constant loss of 10^9 and are therefore discarded by the HyperBand selection. Valid denoiser candidates are ranked by their validation mean-squared-error loss. HyperBand has been used on HGQ models [13] in the case of the classifier and QKeras [23] for the denoiser (see section 3.4).

The result of this optimisation and selection procedure is a compact classifier and a compact

denoiser, which together define the model set used in the remainder of the paper. The classifier represents the decision stage against which the denoiser-assisted trigger can be compared, while the denoiser represents the waveform-cleaning stage selected for the deployment-oriented studies. Figure 5 shows the selected architectures together with their key hyperparameters.

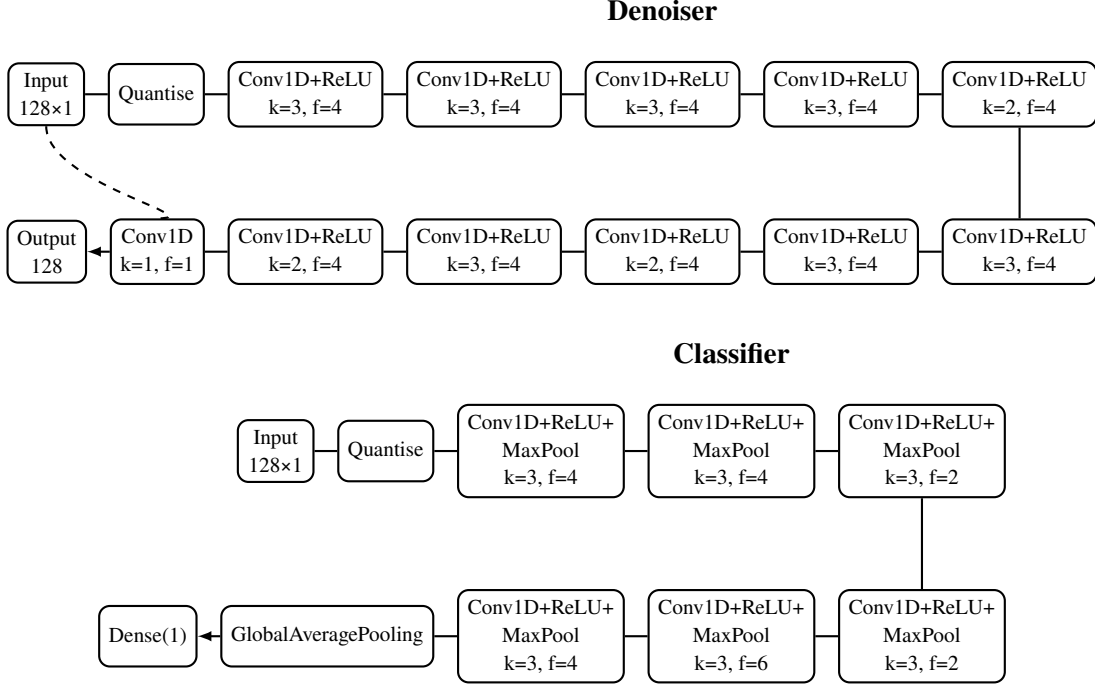


Figure 5: Architecture diagrams of the denoiser (top) and classifier (bottom). The kernel size is abbreviated by k , the number of filters by f . The dashed line denotes a skip connection.

3.4 Quantisation-aware training and high-granularity quantisation

Deployment compatibility is addressed already during training rather than only after the floating-point models are fixed. Quantisation-aware training (QAT) is the central mechanism for this step: the models are trained under fixed-point constraints so that the optimisation sees, at least approximately, the numerical limitations that will later be imposed by the FPGA implementation. This reduces the mismatch between software training and hardware inference and provides a more reliable basis for converting the selected models with `hls4ml` into synthesizable firmware [19–21].

Classifier: The precisions for the weights and activations have been set manually for every layer and can be seen in Table 4. The precisions are of the shape `ap_fixed<t,i,RND,SAT>`, where t stands for the total bits and i stands for the integer bits. The RND and SAT modes specify rounding to the nearest representable value and saturation on overflow, respectively. The granularity for HGQ, described by the β -value, is set to $\beta = 8 \cdot 10^{-6}$.

Denoiser: Here, the bit widths have been set globally to `ap_fixed<14,8,RND,SAT>`, with a $\beta = 8 \cdot 10^{-7}$, as summarised in Table 5.

Both the classifier and denoiser are quantised independently and have been trained quantisation-aware. The hardware impact of the quantisation strategy is quantified in Sec. 5, where the post-implementation resource use, latency, and power of the complete trigger firmware are reported.

Table 4: Final fixed-point precisions used for each classifier block in the high-level synthesis (HLS) implementation.

Block	Type	Layer	Total bits	Integer bits
1	Weight	Conv1D	5	2
1	Bias	Conv1D	4	1
1	Result	Conv1D	14	4
1	Result	ReLU	11	4
1	Result	MaxPool	11	4
2	Weight	Conv1D	6	2
2	Bias	Conv1D	7	1
2	Result	Conv1D	17	6
2	Result	ReLU	13	5
2	Result	MaxPool	13	5
3	Weight	Conv1D	6	2
3	Bias	Conv1D	4	1
3	Result	Conv1D	16	6
3	Result	ReLU	14	6
3	Result	MaxPool	14	6
4	Weight	Conv1D	5	2
4	Bias	Conv1D	7	1
4	Result	Conv1D	16	7
4	Result	ReLU	14	7
4	Result	MaxPool	14	7
5	Weight	Conv1D	7	2
5	Bias	Conv1D	7	2
5	Result	Conv1D	19	8
5	Result	ReLU	15	7
5	Result	MaxPool	15	7
6	Weight	Conv1D	6	2
6	Bias	Conv1D	7	1
6	Result	Conv1D	19	8
6	Result	ReLU	15	7
6	Result	MaxPool	15	7
Head	Result	GAP	15	7
Head	Weight	Dense	6	1
Head	Bias	Dense	6	1
Head	Result	Dense	15	6

Table 5: Global fixed-point precision used for the denoiser HLS implementation.

Denoiser precision policy	Total bits	Integer bits
Global <code>ap_fixed<14,8,RND,SAT></code> precision	14	8

4 Trigger performance

This section compares the trigger branches considered in the present study against the classical threshold reference. The internal logic follows the model variants introduced by the current development workflow: a denoiser-only branch, a classifier-only branch, and the full denoiser–classifier pipeline. Because the signal-containing samples are intentionally shifted toward the near- and sub-threshold regime, all comparisons must be made on the held-out benchmark samples defined in Sec. 2.4.

4.1 Evaluation metrics and operating points

The primary performance metric is the receiver-operating-characteristic (ROC) curve, expressed in terms of the true-positive rate (TPR) for signal traces and the false-positive rate (FPR) for background traces. The area under the curve (AUC) is reported as a compact summary, but the practically relevant comparison is made at fixed operating points, since a station trigger is never operated over the full ROC. Throughout this section, **Validation Dataset 1** provides the main signal-plus-background benchmark, while **Validation Dataset 2** provides the large background-only sample needed for robust low-FPR estimates.

The same operating points are used for all trigger branches: the threshold reference, the denoiser-only branch, the classifier-only branch, and the full denoiser–classifier chain. Unless stated otherwise, the neural ROC curves in this section refer to the quantisation-aware trained HGQ models evaluated in the Keras environment. The corresponding firmware-exported `hls4ml` response is shown explicitly for the full chain as a conversion consistency check. Here, a low FPR_{low} of 10^{-4} has been chosen as a benchmark for very strict false-positive requirements, corresponding to 0.01% of noise-only traces misidentified as signals. The nominal benchmark operating point is $\text{FPR}_{\text{nom}} = 10^{-2} = 1\%$.

4.2 Classical threshold baseline

The classical reference is the same peak-envelope threshold trigger already used in Ref. [12]. For each trace, the analytic signal is formed and the trigger score is derived from the Hilbert-envelope peak together with the corresponding noise normalisation, following the published definition. The threshold branch is evaluated on the same band-pass-filtered traces as the neural branches, so the comparison is performed on one common input representation.

This threshold trigger serves two purposes in the present paper. First, it provides the conventional reference against which the neural methods are compared. Second, it provides the decision stage for the denoiser-only branch described below, where the same peak-envelope threshold is applied after waveform cleaning.

Table 6: Main branch-level trigger comparison. The neural branches improve the trigger classification compared to the baseline peak-envelope trigger by increasing the ROC AUC and the TPR at the nominal and low-FPR operating points.

Trigger branch	AUC	TPR@FPR _{nom}	TPR@FPR _{low}
Threshold baseline	0.629	0.1	0.000
Denoyer-only	0.98	0.87	0.16
Classifier-only	0.984	0.84	0.27
Denoyer + classifier	0.986	0.89	0.41

4.3 Comparison of trigger branches

The following trigger branches are compared to each other:

1. **Denoyer-only:** the trace is first denoised, and the decision is then made by the peak-envelope threshold of Sec. 4.2;
2. **Classifier-only:** the classifier acts directly on the band-pass-filtered raw trace;
3. **Denoyer + classifier (hybrid trigger):** the denoised trace is passed to the classifier.

These three branches isolate the two possible sources of improvement: the denoyer-only branch tests whether waveform cleaning helps a conventional threshold decision, while the classifier-only and denoyer-classifier branches test whether the denoised waveform adds information beyond a direct decision-level classifier. Table 6 summarises the final branch-level trigger comparison. It compares the branch logic itself, separating waveform cleaning from decision-level classification while keeping all operating points common across the threshold baseline, denoyer-only branch, classifier-only branch, and full denoyer-classifier chain.

The ROC figures are organised in the same order as the branch logic. Figure 6 shows whether denoising alone improves the separation obtained with a simple peak-envelope threshold. A peak-envelope trigger that acts on the raw noisy input achieves an AUC of 0.63; after denoising, this value increases to 0.98.

Figure 7 shows the ROC curve of the classifier-only branch. The AUC increases to 0.984 compared to the classical peak-envelope trigger. The classifier also retains signal efficiency in the low-FPR region, where the classical trigger has no remaining accepted signal traces in the present benchmark.

Figure 8 shows the ROC curve of the full denoyer-classifier chain, which we refer to as the hybrid trigger in the following. The hybrid branch reaches an AUC of 0.986 and retains a TPR of about 0.41 at the strict operating point $FPR_{low} = 10^{-4}$. The low-FPR part of the curve shows a plateau near this efficiency before rising toward higher false-positive rates. The `hls4ml` curve closely follows the HGQ/Keras result, with a slightly larger AUC of 0.987 and a TPR of about 0.39 at $FPR_{low} = 10^{-4}$; this small difference is interpreted as a conversion-level effect rather than a real performance gain. Together, these figures show the progression from classical triggering to waveform cleaning and finally to the full hybrid trigger.

The ablation therefore leads to two conclusions. Denoising alone already makes a simple peak-envelope trigger substantially more efficient, demonstrating that the waveform-cleaning stage preserves trigger-relevant signal structure. The full denoiser–classifier chain gives the largest overall AUC and the strongest performance at both the nominal and strict low-FPR operating points, and is therefore the preferred branch for the background-limited trigger regime. The low-FPR operating point is evaluated with the large background-only sample of **Validation Dataset 2**, so that the strict false-positive comparison is not limited by the smaller mixed validation sample.

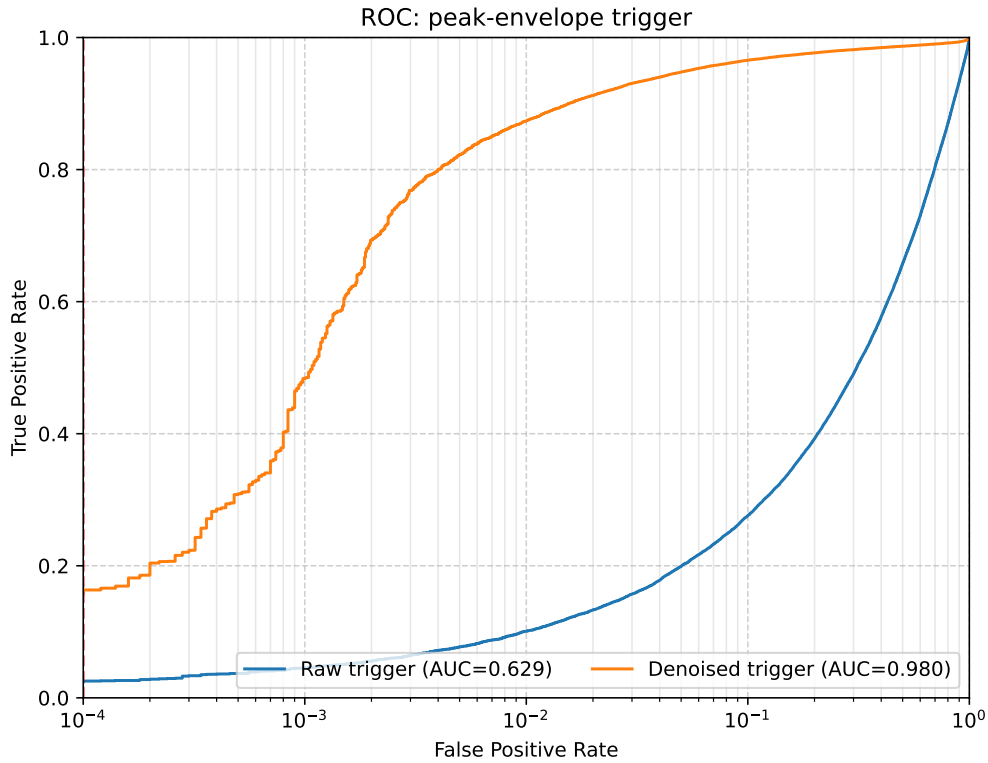


Figure 6: ROC curve of the denoiser-only branch compared with the peak-envelope threshold applied to the raw trace. Applying the same threshold after denoising increases the AUC from 0.63 to 0.98.

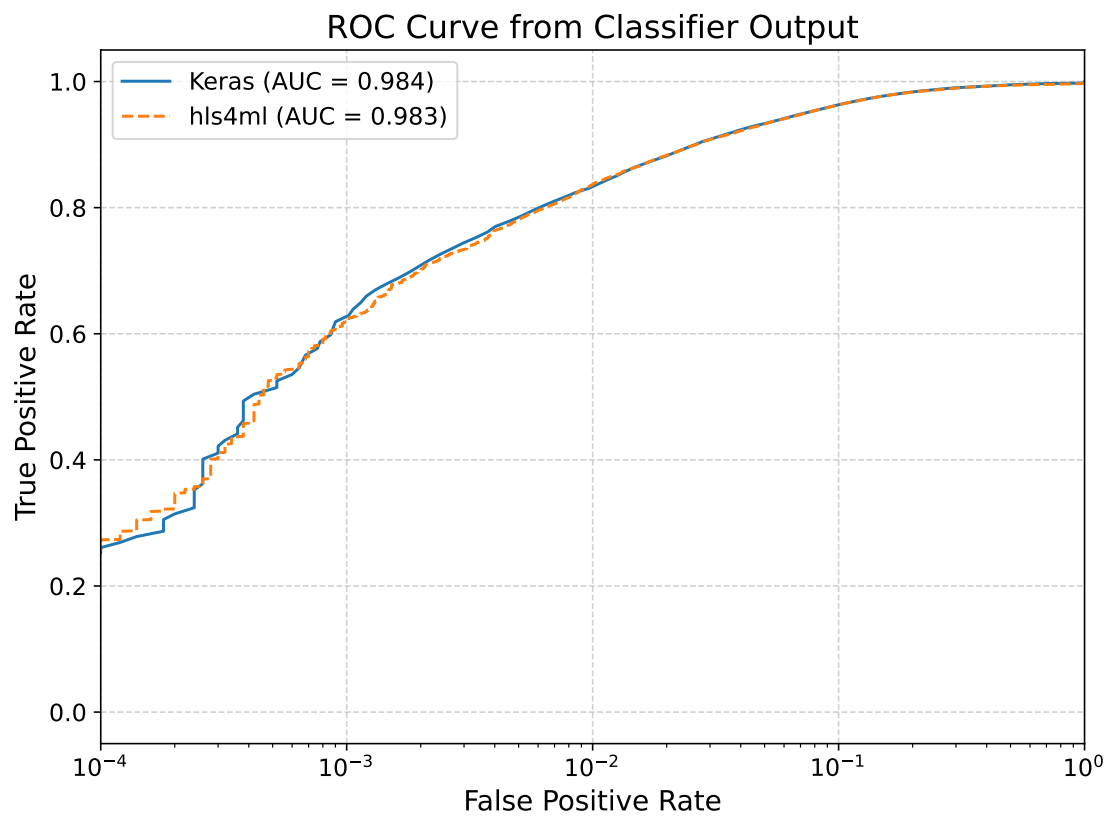


Figure 7: ROC curve of the classifier-only branch. The HGQ/Keras classifier reaches an AUC of 0.984 and maintains signal efficiency at lower false-positive rates than the classical threshold trigger.

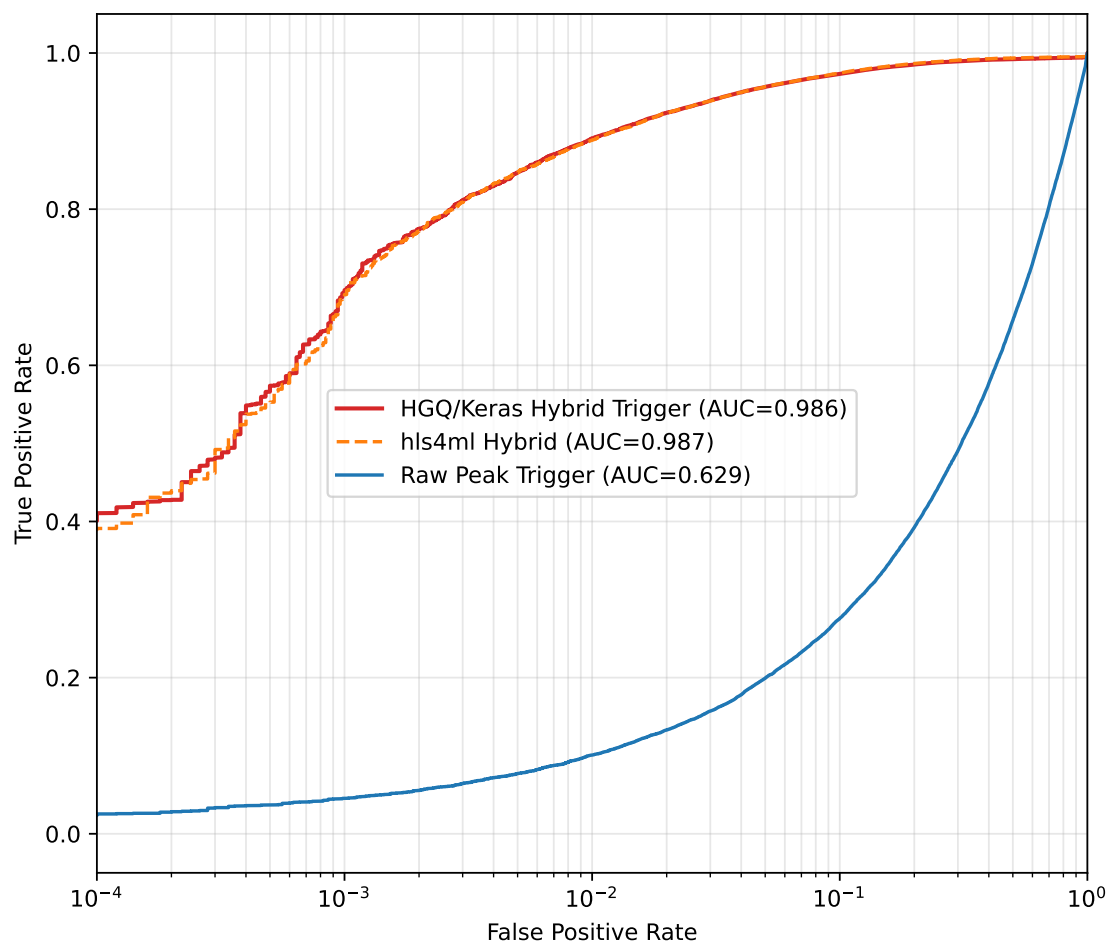


Figure 8: ROC curve of the full denoiser–classifier chain (hybrid trigger) compared with the peak-envelope threshold applied to the raw trace, shown in blue. The HGQ/Keras branch reaches an AUC of 0.986 and gives a TPR of about 0.41 at $FPR_{low} = 10^{-4}$. The hls4ml export closely follows the HGQ/Keras curve, with an AUC of 0.987 and a slightly lower TPR of about 0.39 at $FPR_{low} = 10^{-4}$.

5 FPGA implementation

This section presents the FPGA realisation of the hybrid trigger and quantifies the resulting hardware cost. The key outcome is not only that the model can be synthesised, but that the new pipeline changes the deployment frontier compared with the previously published design. The FPGA implementation uses the QAT/HGQ models described in Sec. 3.4, whose trigger-level agreement with the fixed-point hls4ml representation was verified in figure 8; this section therefore focuses on resource use, timing, latency, and power.

5.1 Target platforms and tool flow

The hardware study follows the same benchmarking logic as the classifier-only implementation in Ref. [12]. Rather than surveying all possible low-cost FPGA families, we use a small set of representative targets to separate station-class feasibility from device-scaling behaviour. The Zynq-7000 Z-7020 is used as the conservative low-resource reference because it represents the scale of compact station-level FPGA fabrics. It should therefore be read as a stress test of the implementation, not as a prescription for the final deployment device. Larger FPGA targets are included to show how the same generated design scales when more routing, memory, and DSP resources are available. The resulting resource and timing summary is given in Table 7.

The trained QAT/HGQ denoiser and classifier are converted from the Keras model description to a fixed-point HLS representation with hls4ml [19–21]. The generated HLS design is synthesised with Vitis HLS 2024.1 [24], targeting the representative FPGA platforms listed in Table 7. For the post-implementation study, the FPGA timing constraint was relaxed to 6 ns to obtain robust timing closure on the most constrained target, the Zynq-7000 Z-7020, using the unmodified register-transfer-level (RTL) design generated by hls4ml. This implementation clock only sets the internal processing rate used for hardware timing and latency estimates; it does not change the physics sampling assumptions of the input traces. Since the remaining timing pressure is marginal, further timing-oriented HLS or RTL pipelining would be expected to reduce this constraint, but such device-specific optimisation is outside the scope of the present comparison. The following subsections report the hardware cost of the complete denoiser–classifier trigger chain; any differences between the HGQ/Keras and hls4ml responses have already been checked at trigger level in Sec. 4.3.

After HLS synthesis, the denoiser and classifier are exported as separate RTL intellectual-property (IP) blocks and assembled in a Vivado 2024.1 block design [25]. The design contains the two hls4ml-generated IP cores, the top-level wiring between them, and the clock, reset, start, and ready/control logic required to exercise the chain. The denoiser IP receives the 16-bit input stream and its output is connected to the classifier input, so that the implemented design corresponds to the complete denoiser–classifier trigger path. The resource, latency, timing, and power values reported below are obtained after Vivado synthesis and implementation, including placement, routing, and timing closure for each target device. For the standalone hardware test design, the input stream is generated by a 16-bit pseudo-random binary sequence (PRBS) source. The PRBS block is implemented as a linear-feedback shift register initialised to all ones. On each clock cycle, the register is shifted by one bit and the feedback bit is

$$b_{fb} = b_{15} \oplus b_{13} \oplus b_{12} \oplus b_{10},$$

Table 7: Post-implementation resource use, latency, and timing closure for the full denoiser–classifier design on representative FPGA targets. LUT denotes lookup-table resources, FF denotes flip-flop resources, and BRAM denotes block random-access memory. The Z-7020 is used as the conservative low-resource reference, while the larger devices show scaling behaviour and timing headroom.

Platform	LUT	FF	BRAM	DSP	Latency [μ s]	Timing met
Zynq-7000 Z-7020	22 906	39 817	50	42	13.55	yes
Kintex UltraScale xcku040	22 624	25 370	31.5	68	5.66	yes
Alveo U250 xcu250	22 287	20 777	32	70	3.63	yes

corresponding to taps of the polynomial $x^{16} + x^{14} + x^{13} + x^{11}$. This source is not part of the physics trigger chain itself and is not used for the end-to-end RTL validation in Sec. 5.4. It is included only in the standalone implementation setup used to drive non-constant activity when assessing post-implementation resource use and dynamic power.

5.2 Resource use, timing, and power

Table 7 summarises the post-implementation results for the complete denoiser–classifier trigger chain on the representative FPGA targets. Placed-and-routed designs include routing, packing, and timing-closure effects that are not visible in high-level synthesis estimates alone, and are therefore the relevant quantities for assessing implementation feasibility.

The Z-7020 row is the most conservative one: its resource use should be interpreted as implementation pressure on a constrained reference device, not as a universal resource estimate for the model. Conversely, the larger targets provide additional DSP, memory, and routing headroom, which is reflected in the reduced latency and continued timing closure. The end-to-end latency decreases from 13.55 μ s on the Z-7020 to 5.66 μ s on the Kintex UltraScale target and 3.63 μ s on the Alveo U250, while all three implementations meet the imposed timing constraint after placement and routing.

The quoted dynamic-power values used for the comparison with the previous FPGA study are discussed in Sec. 5.3. These values are obtained from the post-implementation FPGA power analysis using the activity model of the implemented design, providing a consistent design-level comparison across the target devices.

5.3 Hardware-cost reduction relative to the published FPGA study

Table 8 compares the present design with the previously published FPGA implementation of Ref. [12]. The resource comparison is made for the same target FPGA, the Zynq-7000 Z-7020. For the published design, however, the quoted resource numbers correspond to the post-synthesis report, because that design could not be placed and routed on the Z-7020. In contrast, the current design reaches implementation on the Z-7020. The dynamic-power estimates are therefore listed separately for the Z-7020 and for the Alveo U250, so that the station-class implementation result and the direct comparison to the published Alveo implementation are both visible.

Table 8: Comparison of FPGA resource demand and dynamic-power estimates for the published FPGA implementation and the current deployment-oriented hybrid trigger design. Resource numbers are quoted for the Zynq-7000 Z-7020 target in both cases. The published design could not be implemented on the Z-7020, so no Z-7020 dynamic-power estimate is available for that row; the U250 column gives the direct power comparison to the device used in Ref. [12].

Design	Resource report	DSP	LUT	BRAM	Z-7020 dyn. power [W]	U250 dyn. power [W]
Published FPGA study [12]	post-synthesis on Z-7020	2119	191243	780	–	5.51
Current design	post-implementation on Z-7020	42	22920	50	0.562	0.270

The most important change is the DSP demand on the Z-7020 target, which drops from 2119 blocks at post-synthesis level in the published study to 42 blocks after implementation in the current design. Since DSP availability was the dominant bottleneck in the earlier FPGA study, this reduction directly changes the feasibility of deploying the trigger on constrained station-level hardware. The dynamic-power comparison on the Alveo U250, the device used for the published implementation, decreases from 5.51 W to 0.270 W. The current design also implements directly on the Z-7020, where the post-implementation dynamic-power estimate is 0.562 W. LUT and BRAM usage follow the same downward trend, supporting the conclusion that the present design is not merely a performance extension of the previous study, but a substantially cheaper hardware implementation.

5.4 End-to-end RTL validation

Beyond synthesis and implementation reports, the design response is validated at the RTL level with a Python-based `cocotb` testbench [26]. The purpose of this step is to verify that the generated hardware logic preserves the model response when driven with representative traces, rather than only checking that the design can be synthesised. The testbench applies the same input normalisation used in the software validation, evaluates the quantised reference model at Python/`hls4ml` level, drives the VHDL design in simulation, and records the resulting RTL trigger probabilities.

The RTL simulation is computationally more expensive than the software-level studies, so the end-to-end comparison is performed on a balanced validation subset containing 2000 signal traces and 2000 background traces. The absolute AUC values obtained on this subset should therefore not be compared one-to-one with the full-statistics curves in Sec. 4. The relevant validation here is instead the comparison between the `hls4ml` reference and the RTL output on the same events.

Figure 9 first checks the denoiser output at waveform level. For the representative trace shown, the `hls4ml` and RTL outputs have a correlation coefficient of 99.5%, and the residual remains small compared with the coherent pulse amplitude. This event-level check verifies that the RTL simulation of the generated design preserves the denoised trace shape that is passed to the classifier.

The trigger-level validation is shown in figure 10. The ROC curves from the RTL simulation and the `hls4ml` reference nearly overlap over the full false-positive-rate range, with AUC values of 0.966 and 0.968, respectively. This small difference is consistent with the finite validation subset and the numerical details of the RTL realisation. More importantly, the agreement is evaluated event-by-event on the same traces, showing that the hardware-realised trigger preserves the signal-background ordering of the quantised software reference. The floating-point and HGQ/Keras

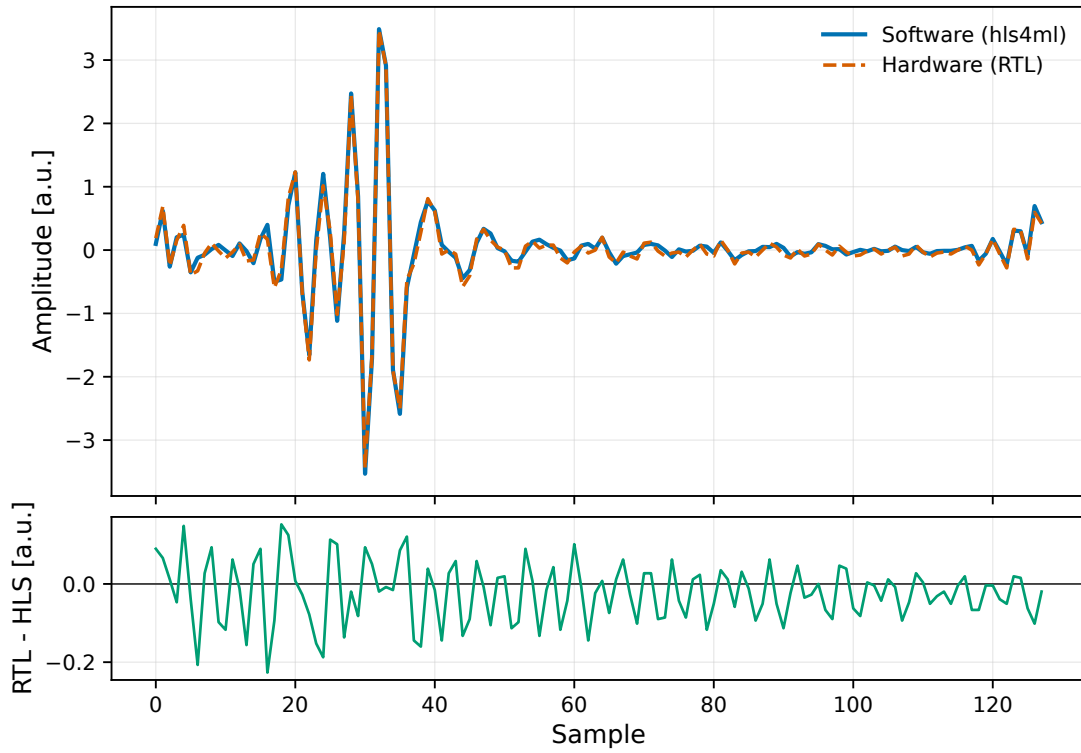


Figure 9: Event-level RTL validation of the denoiser output for a representative trace. The hls4ml reference and RTL waveform agree with a correlation coefficient of 99.5% for the example shown; the lower panel shows the residual between the RTL and hls4ml outputs.

comparisons are not repeated here, since their agreement with the hls4ml model has already been established in Sec. 4.3.

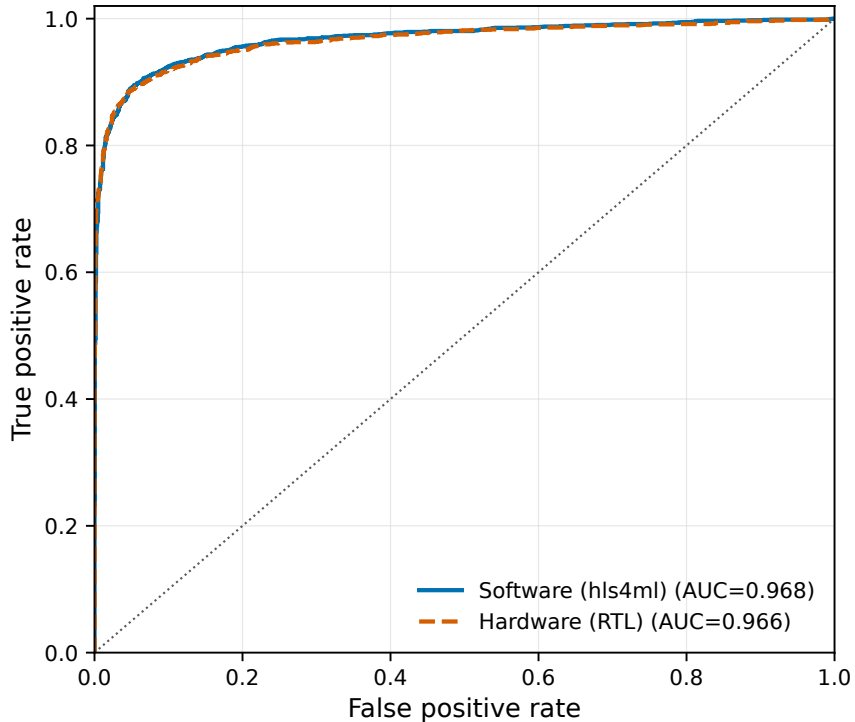


Figure 10: ROC-level validation of the end-to-end RTL simulation against the quantised hls4ml reference on the balanced RTL validation subset containing 2000 signal traces and 2000 background traces. The software reference gives an AUC of 0.968, while the RTL simulation gives an AUC of 0.966.

6 Discussion

The trigger and hardware results address the same instrumentation question from complementary directions: whether waveform denoising can improve autonomous radio triggering without exceeding the resource envelope of an edge FPGA implementation. The discussion therefore focuses on the gain in recoverable weak traces at fixed background load, the additional information carried by the denoised waveform beyond a decision-level score, and the deployment steps needed to translate the demonstrated station-level trigger block into a broader radio-array readout strategy.

6.1 Physics and operational implications

The trigger comparison developed in Sec. 4.3 is most directly interpreted through the recovery of weak signal-containing traces at fixed background load. This is the operating regime that limits autonomous radio triggering, because conservative thresholds suppress precisely the low-amplitude pulses that are most vulnerable to noise fluctuations. For this purpose, we compare the hybrid trigger directly to the threshold baseline. The signal-strength coordinate is the same revised analysis-side proxy introduced in Eq. 2.1. Writing

$$\rho \equiv \log_{10}(\text{SNR}), \quad (6.1)$$

we bin the held-out **Validation Dataset 1** in ρ and evaluate, in identical bins, the signal efficiencies of the threshold branch and the hybrid branch. The operating thresholds of the two branches are chosen independently on held-out background traces so that both correspond to the same target false-positive rate. This yields two directly comparable efficiency curves, $\epsilon_{\text{base}}(\rho)$ and $\epsilon_{\text{hyb}}(\rho)$, under matched background conditions.

The most compact physics-facing summary is then the conditional detection gain

$$G(\rho) \equiv \frac{\epsilon_{\text{hyb}}(\rho)}{\epsilon_{\text{base}}(\rho)}. \quad (6.2)$$

By construction, $G(\rho) > 1$ identifies signal-strength bins in which the hybrid trigger recovers traces that would be missed by the classical threshold trigger at the same background load. Bins in which the baseline efficiency is consistent with zero do not admit a stable finite ratio and should therefore not be overinterpreted.

Figure 11 therefore answers the station-level trigger question directly: within the validated signal-strength range of the benchmark, how much extra near-threshold radio content becomes available to a radio-only trigger path when the hybrid trigger is applied?

Within this formulation, the physics implication is immediate. Any systematic increase in $G(\rho)$ over a finite low- ρ interval corresponds to a proportional increase in the number of detectable signal-containing traces in precisely the regime that limits autonomous radio triggering. The hybrid trigger therefore relaxes an instrumental limitation that otherwise forces conservative thresholds and suppresses weak events.

At the fixed false-positive operating point of 10^{-2} , the conditional detection gain is substantial throughout the weak-signal regime. In the lowest finite bin shown in figure 11, centred at $\rho = -0.158$, the gain is $G = 63.2^{+52.1}_{-26.8}$, where the asymmetric uncertainty follows from Clopper–Pearson intervals propagated to the efficiency ratio. Even at the upper end of the plotted finite range, $\rho = 0.993$, the gain remains $G = 5.46^{+0.73}_{-0.64}$. These values show that the hybrid trigger provides a strong multiplicative increase in recoverable near-threshold events, rather than a marginal improvement, precisely in the regime that limits autonomous radio triggering.

This same low- ρ gain is the part of the result with the clearest relevance for inclined and otherwise radio-faint geometries. Such events deposit less per-station amplitude and are therefore disproportionately exposed to efficiency losses from conservative thresholding. A trigger branch that preserves more efficiency in the weak-signal bins at fixed background rate removes part of that bias at the station level, even before any array-level acceptance study is attempted.

6.2 What the denoiser adds beyond a decision-level trigger

The classifier-only branch is a strong benchmark because it already uses waveform information before making a binary decision. The question is therefore not whether a neural decision stage is useful, but whether an explicit waveform-regression stage adds information that cannot be reduced to another decision-level score. The ablation in Table 6 gives the most direct answer. At the nominal operating point, the classifier-only and full denoiser–classifier branches have comparable efficiencies, with TPR values of 0.84 and 0.89, respectively. The denoiser is therefore not introduced because the classifier-only branch fails at loose background conditions, but because it improves the trigger response across the benchmark while also providing a cleaned waveform. At $\text{FPR}_{\text{low}} = 10^{-4}$,

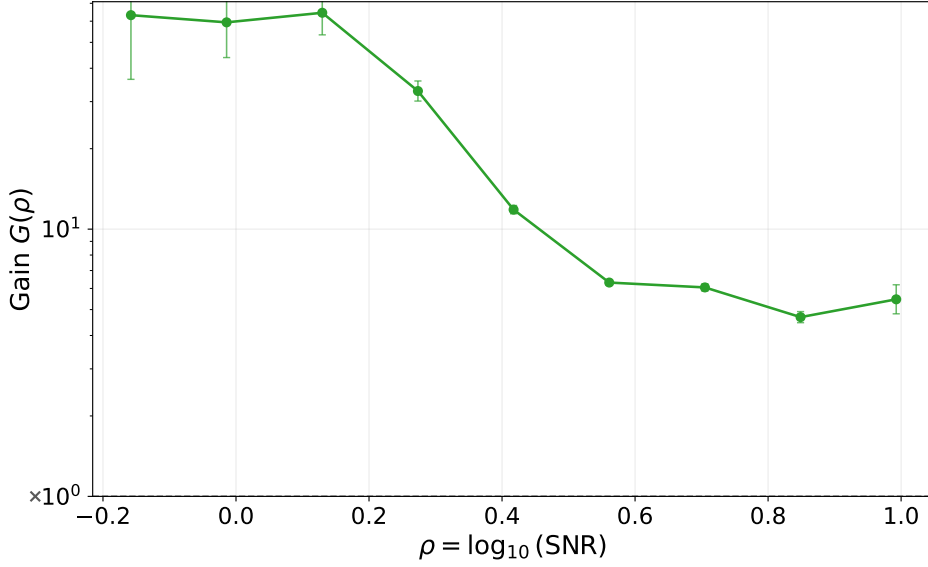


Figure 11: Efficiency gain $G(\rho) = \epsilon_{\text{hyb}}(\rho)/\epsilon_{\text{base}}(\rho)$ as a function of the signal-strength proxy $\rho = \log_{10}(\text{SNR})$ for the hybrid trigger relative to the threshold baseline, evaluated at a fixed false-positive rate of 10^{-2} . The curve quantifies the relative increase in detectable signal-containing traces in the near-threshold regime.

the classifier-only branch reaches a TPR of 0.27, while the full denoiser–classifier branch reaches about 0.41.

This behaviour is consistent with the denoiser-only branch. If the same peak-envelope threshold is applied after waveform cleaning, the AUC increases from 0.63 for the raw threshold trigger to 0.98 for the denoised threshold trigger. This is an important control test because the downstream decision rule is then deliberately simple. The improvement cannot be attributed to a more flexible classifier head; it shows that the denoiser changes the waveform representation itself by suppressing noise excursions while preserving pulse-like structure.

The denoiser also provides a diagnostic object that a pure classifier does not: a cleaned trace that can be inspected, thresholded, compressed, or passed to other station-level logic. This is relevant beyond the single-station trigger score. In a bandwidth-limited radio array, the station does not only need to decide whether a trace is interesting; it may also need to transmit a compact set of features, such as pulse time, peak amplitude, or integrated envelope, to support array-level coincidence building, direction reconstruction, quality cuts, or selective waveform readout. A classifier-only trigger can provide a probability, but it does not by itself produce a waveform from which these features can be extracted with a simple and auditable edge algorithm.

Figure 12 therefore tests the denoised waveform as an edge-processing product rather than only as an input to the classifier. The timing panel gives the residual between the envelope-peak position after denoising and the envelope-peak position of the paired pure pulse. Its concentration around zero supports the interpretation that the denoiser preserves the pulse location rather than

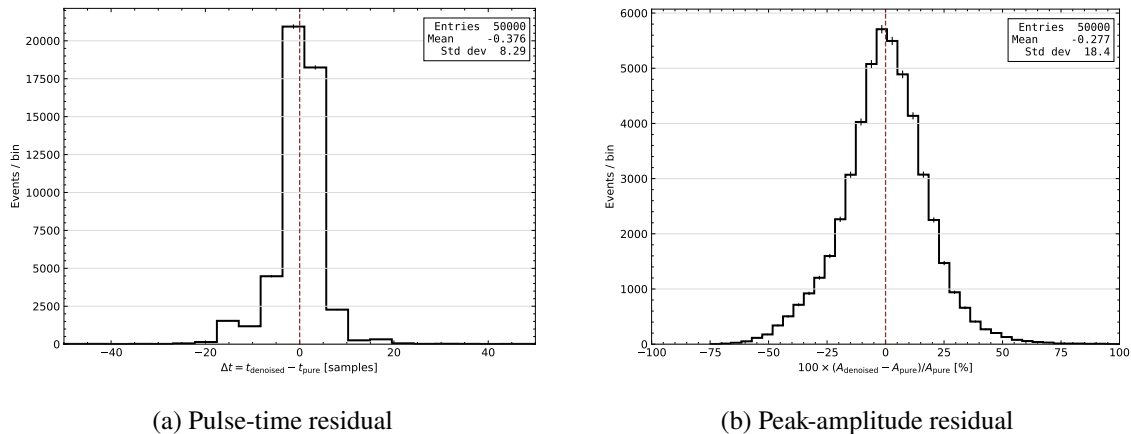


Figure 12: Event-by-event feature residuals for denoised signal traces relative to the paired pure signal pulse. The timing residual tests whether the denoiser preserves the pulse position, while the amplitude residual tests whether the cleaned waveform keeps the pulse scale without relying on the downstream classifier score.

merely suppressing large samples. The amplitude panel shows the corresponding peak-amplitude residual after denoising. The distribution is centred close to zero but has a finite width, which is the waveform-level origin of the residual spread summarised below in Table 9. These tails are important because fixed-threshold and feature-transmission schemes are usually controlled by the worst-behaved part of the distribution, not only by the mean response.

For the feature diagnostics, the denoised output is first mapped back to trace units using the z-score scale of the corresponding signal trace. The amplitude scale is then adjusted in post-analysis by one global factor, chosen from the median peak response of the denoised validation traces relative to their paired pure signal traces. This calibration is used only to display and quantify the denoised waveform in trace units; it is not used by the trigger decision or by the ROC curves. The timing residual is largely insensitive to such an overall amplitude rescaling, whereas the peak-amplitude and integrated-envelope diagnostics should be interpreted with this diagnostic calibration convention.

The same feature information can be compressed into the aggregate comparison in Table 9. Before denoising, the peak-amplitude response is biased high by the noise contribution, with a mean response factor of 1.92 and a median response factor of 1.91. After denoising, the mean peak-amplitude response is 0.997 and the median is 1.00. The pulse-time residual also improves, from a standard deviation of 41.3 samples for the raw trace to 8.29 samples after denoising, with the median residual reduced from one sample to zero. The integrated-envelope response remains above unity after denoising, with a mean value of 1.23, so the denoised waveform should not be interpreted as a precision calorimetric reconstruction. For triggering and edge preprocessing, however, the relevant result is that the dominant timing and peak-amplitude distortions of the raw trace are substantially reduced.

The corresponding sample-level residual distributions are shown in figure 13. For each trace, the residual is normalised by the RMS of the relevant raw noise contribution: the raw noise trace

Table 9: Aggregated waveform-level diagnostics for the denoiser on held-out signal traces. The raw noisy trace and the denoised trace are each compared to the paired pure signal target. Entries with scale “samples” are signed differences in pulse position, while entries with scale “ratio” are dimensionless response ratios relative to the paired target quantity. These quantities are diagnostic only and are not used to define the trigger operating thresholds.

Diagnostic quantity	Raw signal vs. truth	Denoised vs. truth	Scale
Pulse-time residual, mean	2.18	-0.38	samples
Pulse-time residual, std. dev.	41.3	8.29	samples
Pulse-time residual, median	1.00	0.00	samples
Peak-amplitude response, mean	1.92	0.997	ratio
Peak-amplitude response, std. dev.	0.316	0.184	ratio
Peak-amplitude response, median	1.91	1.00	ratio
Integrated-envelope response, mean	6.25	1.23	ratio
Integrated-envelope response, median	5.07	1.13	ratio

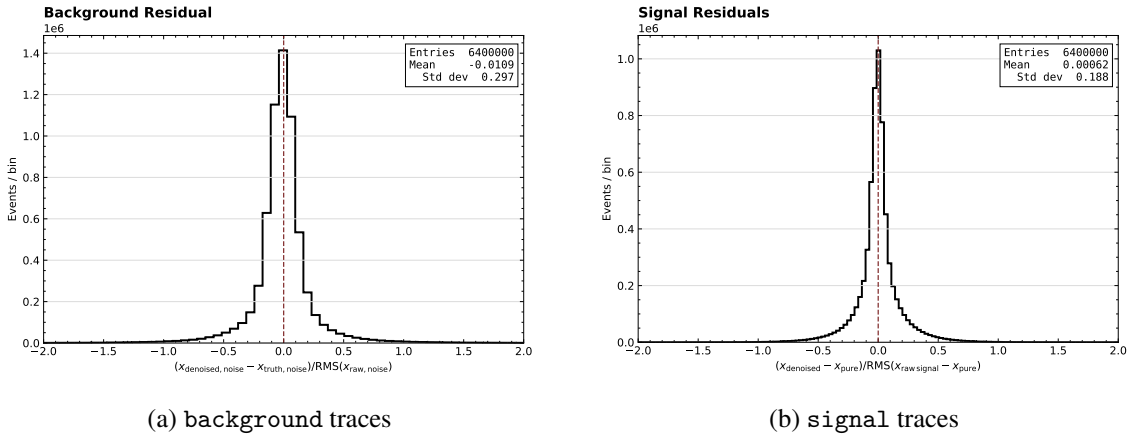


Figure 13: Normalised sample-level denoiser residuals. For background traces the target is zero output and the residual is divided by the raw-noise RMS. For signal traces the residual is computed relative to the paired pure signal pulse and divided by the RMS of the injected noise contribution.

for background samples and the difference between the raw signal trace and the paired pure signal pulse for signal-containing samples. The noise-only panel therefore tests the failure mode that is most relevant for a trigger, namely whether the denoiser creates signal-like structure from background traces. Over 6 400 000 samples, the residual distribution has a mean of -0.0109 and a standard deviation of 0.297 in units of the raw-noise RMS. The signal panel shows the residual between the denoised waveform and the paired pure pulse, normalised in the same way to the injected noise contribution; its mean is 6.2×10^{-4} and its standard deviation is 0.188 . The small biases and sub-noise RMS widths in both panels support the interpretation that the denoiser suppresses noise while preserving the pulse, rather than acting as an unconstrained pulse generator.

The practical gain is therefore twofold. First, denoising improves the trigger response when used before the classifier, increasing both the integrated AUC and the fixed-FPR efficiencies relative

to the classifier-only branch. Second, the cleaned waveform is an intermediate data product. It can support simple peak-envelope decisions, timing diagnostics, event-quality checks, or selective waveform readout, whereas a decision-level trigger only returns a score. This distinction is important for bandwidth-constrained autonomous radio stations: the denoiser is not only another way to make the same binary decision, but a compact front-end transformation that makes weak pulses more accessible to both the trigger and the downstream readout logic.

6.3 Limitations and robustness checks

The implemented chain demonstrates that the denoiser–classifier trigger can run with the normalised trace representation required by the HGQ-based quantised models used here. For deployment, this normalisation should be treated as part of the trigger interface: the station trigger must either receive or compute the same representation used during model validation. For a compact quantised FPGA trigger, the amplitude range and normalisation rule define the numerical range seen by the neural models. The deployment version can therefore specify this interface together with the firmware, using for example station-level pedestal and scale constants, a cheaper fixed calibration scheme, or a retrained/exported model variant operating on calibrated ADC-scale inputs. This normalisation interface is also a near-term hardware optimisation opportunity. The resource numbers reported for the implemented full chain include the normalisation stage, so the quoted DSP count should be interpreted as the cost of the realised trigger path rather than of the denoiser and classifier convolutional core alone. Reducing the arithmetic cost of the normalisation stage would lower the full-chain DSP demand without changing the basic denoiser–classifier architecture.

The same interface matters if the denoised waveform is used beyond the station-level trigger decision. The timing diagnostics in Sec. 6.2 test whether denoising preserves the pulse position, which is the waveform feature most relevant for possible array-level, polarisation-level, or multi-channel coincidence logic. For peak-amplitude and integrated-envelope features, a deployment implementation should either remove the normalisation step by exporting a model that operates on calibrated ADC-scale inputs, or define the inverse scale from station calibration and background-monitoring quantities available in the firmware. This would replace the present analysis-side amplitude calibration with an operational calibration path and allow the waveform-level validation to be repeated directly in deployment units for feature-only readout, selective waveform buffering, and other bandwidth-saving modes.

The signal benchmark is intentionally weighted toward weak traces. This choice provides a stress test of the operating regime in which a radio-only trigger is most constrained. The earlier classifier-only trigger already performs well for high-SNR pulses, whereas the relevant question for the present work is whether denoising recovers efficiency close to threshold at fixed background rate. The main trigger conclusion is therefore taken from the fixed-FPR efficiency comparison against the same threshold baseline, the improved integrated ROC performance, and the dependence of this gain on signal strength.

We checked the stability of this conclusion with two alternative signal mixtures. A validation sample shifted toward higher signal strengths, spanning approximately $-0.8 \lesssim \log_{10}(\text{SNR}) \lesssim 2.7$, gives the expected behaviour: the raw peak-envelope threshold trigger improves because the sample contains fewer near-threshold traces, while the hybrid branch remains more efficient, with an absolute TPR increase of about 33 percentage points at $\text{FPR} = 10^{-4}$. In a second check, the

event-by-event amplitude scan was replaced by a single global scale factor applied to the detector-level pulse library, leaving the natural relative pulse-amplitude variation of the simulated traces unchanged. This sample has a different signal-strength composition and is therefore not expected to reproduce the benchmark efficiency curve bin by bin. The relevant observation is instead that the trigger ordering is preserved. In common signal-strength bins with sufficient statistics, the hybrid efficiency remains several times larger than the raw peak-trigger efficiency; representative overlapping bins at the nominal FPR of 10^{-2} give hybrid efficiencies of about 0.68–0.89, compared with raw peak-trigger efficiencies of about 0.07–0.10, corresponding to gains of order 7–9. These checks support the interpretation that the observed hybrid-trigger advantage is not an artefact of the particular near-threshold amplitude weighting used for the main benchmark, while the absolute efficiency values remain tied to the stated benchmark definition.

The background validation should also be extended toward detector generalisation. The measured-noise sample used here is valuable because it provides a controlled comparison to the earlier classifier-only trigger under a deliberately difficult interference environment. In a deployed radio array, however, stations may operate under heterogeneous noise conditions due to site-dependent RFI, antenna and electronics differences, seasonal variations, and time-dependent interference. A natural next study is therefore to test the same fixed-FPR protocol across multiple stations and data-taking periods, and to compare a single globally trained trigger with deployment strategies that include station-level calibration constants, periodic retraining, domain adaptation, or controlled online updates based on background data streams. This would address the practical question of how much model adaptation is needed to preserve the demonstrated low-FPR trigger gain across a heterogeneous detector.

Finally, the present trigger is deliberately formulated as a single-channel, fixed-window edge block. This is the right level for isolating the effect of denoising on the waveform and for producing a compact FPGA implementation. A station or array deployment can add further information, including multi-antenna coincidence, polarisation, station geometry, and timing consistency across channels. The denoised waveform is useful in that extension because it can support not only a station-level decision, but also feature-only readout, selective waveform buffering, and compact feature transmission to an array-level trigger in a streaming setup with realistic buffering, threshold updates, deadtime, and DAQ constraints. Translating the resulting station-level gain into detector exposure or event rate is then a separate array-level study.

7 Summary and outlook

This paper has developed a hybrid neural trigger for autonomous radio detection of extensive air showers in a high-interference environment. The central idea is to move the trigger from a pure decision problem to a waveform-recovery problem followed by a decision: a compact denoiser first suppresses the measured radio background and recovers the air-shower pulse candidate, and a compact classifier then evaluates the cleaned trace. The trigger is studied on a deliberately difficult benchmark built from measured noise and detector-folded simulated pulses from the Pierre Auger *Offline* chain, with the signal population concentrated in the near- and sub-threshold regime where autonomous radio triggering is most constrained.

The resulting comparison shows why the denoiser is not merely an auxiliary preprocessing layer. When the same peak-envelope decision is applied after denoising, the area under the receiver-operating-characteristic curve rises from 0.63 for the raw trace to 0.98 for the denoised trace. This control test isolates the waveform-cleaning stage from the classifier and shows that the denoiser changes the trace representation in a trigger-relevant way. In the full denoiser–classifier chain, the hybrid trigger improves the overall ROC performance and the fixed-FPR efficiencies: at a false-positive rate of 10^{-4} , it retains about 41% of the held-out signal traces in the weak-signal benchmark, compared with 27% for the classifier acting directly on the raw trace and no accepted signal traces for the peak-envelope threshold reference.

The cleaned waveform is also a useful station-level data product. Noise-only validation shows that the denoiser suppresses background traces without producing signal-like pulse structure, while signal-trace diagnostics show that the pulse time and peak-amplitude response are substantially stabilised relative to the raw waveform. The timing residual width decreases from 41.3 samples before denoising to 8.29 samples after denoising, and the median peak-amplitude response after denoising is consistent with unity under the current analysis-side normalisation. This does not make the denoiser a precision energy-reconstruction tool, but it does make the cleaned trace useful for timing checks, quality flags, feature-only readout, selective waveform transmission, and downstream coincidence logic.

A second part of the contribution is the deployment workflow. The denoiser and classifier are not selected only for floating-point performance and then compressed afterwards. Hyperparameter optimisation, model-size constraints, quantisation-aware training, high-granularity fixed-point quantisation, hls4ml export, high-level synthesis, and register-transfer-level validation are used as a connected development chain. The implemented firmware preserves the software trigger response and reaches placed-and-routed implementations on representative field-programmable gate array targets. The constrained reference implementation meets the timing target with microsecond-scale latency and uses only tens of dedicated arithmetic blocks, demonstrating that the hybrid trigger is not only a physics-motivated algorithm but also a realistic edge-hardware design.

The main limitations define the next steps. The trace normalisation and inverse-normalisation convention must be fixed as part of the firmware interface, preferably through station-level calibration constants or a model trained directly in calibrated trace units. The background validation should be extended across sites, antennas, electronics chains, seasons, and time-dependent interference conditions to determine how much retraining or domain adaptation is needed. Finally, the single-channel fixed-window trigger should be embedded in a station- and array-level architecture that includes polarisation, multi-antenna timing consistency, buffering, deadtime, threshold updates, and data-acquisition constraints.

Within the scope of this study, the conclusion is that hybrid neural denoising provides both a more sensitive weak-pulse trigger representation and a deployable field-programmable gate array workflow. This makes it a concrete route toward radio-only self-triggering for inclined and otherwise radio-faint air showers in environments where conventional threshold triggers are limited by radio background.

Acknowledgments

The authors gratefully acknowledge the support of the Electronics Laboratory of the Department Physik at Universität Siegen for assistance with the experimental electronics, laboratory infrastructure, and hardware-oriented validation work that underpins the measured-noise and FPGA studies. We thank Prof. Katie Mulrey and Prof. Harm Schoorlemmer for providing the antenna used in the measurement campaign, and Noah Siegemund for assistance with the hardware setup on campus.

We acknowledge the Pierre Auger Collaboration for the simulation and detector-response tools on which the detector-aware signal construction is based, and for the air-shower simulation framework used to produce the detector-folded pulse library. We thank the hls4ml team, and in particular Enrico Lupi, for helpful discussions on the use and configuration of hls4ml. We also acknowledge the developers and maintainers of the open-source software used throughout this work, including Python, NumPy, SciPy, Matplotlib, TensorFlow/Keras, QKeras, hls4ml, cocotb, Vitis HLS, and Vivado.

References

- [1] PIERRE AUGER collaboration, A. Aab et al., *The pierre auger cosmic ray observatory*, *Nucl. Instrum. Meth. A* **798** (2015) 172.
- [2] TELESCOPE ARRAY collaboration, T. Abu-Zayyad et al., *The surface detector array of the telescope array experiment*, *Nucl. Instrum. Meth. A* **689** (2012) 87.
- [3] F.G. Schröder, *Radio detection of cosmic-ray air showers and high-energy neutrinos*, *Prog. Part. Nucl. Phys.* **93** (2017) 1.
- [4] T. Huege, *Radio detection of cosmic ray air showers in the digital era*, *Phys. Rep.* **620** (2016) 1.
- [5] F. D. Kahn and I. Lerche, *Radiation from cosmic ray air showers*, *Proc. R. Soc. Lond. A* **289** (1966) 206.
- [6] E. Conti and G. Sartori, *On the coherent emission of radio frequency radiation from high energy particle showers*, *Int. J. Mod. Phys. D* **26** (2017) 1750083.
- [7] PIERRE AUGER collaboration, A. Abdul Halim et al., *Radio measurements of the depth of air-shower maximum at the pierre auger observatory*, *Phys. Rev. D.* **109** (2024) .
- [8] PIERRE AUGER collaboration, A. Aab et al., *Energy estimation of cosmic rays with the engineering radio array of the pierre auger observatory*, *Phys. Rev. D.* **93** (2016) .
- [9] A. Schmidt, *Realization of a self-triggered detector for the radio emission of cosmic rays*, Ph.D. thesis, Karlsruhe Institut für Technologie (KIT), 2011. 10.5445/IR/1000030957.
- [10] CODALEMA collaboration, D. Torres Machado et al., *Latest results of the CODALEMA experiment: cosmic rays radio detection in a self trigger mode*, *J. Phys. Conf. Ser.* **409** (2013) 012074.
- [11] J. Kelley, *Data acquisition, triggering, and filtering at the auger engineering radio array*, *Nucl. Instrum. Methods Phys. Res. A* **725** (2013) 133.
- [12] Q. Dorosti, *AI-enhanced self-triggering for extensive air showers: performance and FPGA feasibility*, *JINST* **20** (2025) P10010 [2502.21198].
- [13] C. Sun et al., *HGQ: High granularity quantization for real-time neural networks on FPGAs*, *Proc. ACM/SIGDA Int. Symp. Field Programmable Gate Arrays* (2026) 79.

- [14] S. Argirò et al., *The offline software framework of the pierre auger observatory*, *Nucl. Instrum. Methods Phys. Res. A* **580** (2007) 1485.
- [15] PIERRE AUGER collaboration, B. Fuchs, *The auger engineering radio array*, *Nucl. Instrum. Meth. A* **692** (2012) 93.
- [16] PIERRE AUGER collaboration, T. Huege et al., *Determination of the energy scale of cosmic ray measurements using the auger engineering radio array*, *Proc. PoS(ICRC2025)* (2025) 292.
- [17] ICECUBE collaboration, F. Schröder et al., *Application of machine learning to identify radio pulses of air showers at the south pole*, *Proc. PoS(ARENA2024)* (2024) 034.
- [18] ICECUBE collaboration, R. Abbasi et al., *Identification and denoising of radio signals from cosmic-ray air showers using convolutional neural networks*, *Phys. Rev. D* (2026) [2508.14711].
- [19] FastML Team, *fastmachinelearning/hls4ml*, [10.5281/zenodo.1201549](https://doi.org/10.5281/zenodo.1201549) (2025) .
- [20] J. Duarte et al., *Fast inference of deep neural networks in FPGAs for particle physics*, *JINST* **13** (2018) P07027 [1804.06913].
- [21] T. Aarrestad et al., *Fast convolutional neural networks on FPGAs with hls4ml*, *Mach. Learn. Sci. Tech.* **2** (2021) 045015 [2101.05108].
- [22] L. Li et al., *Hyperband: A novel bandit-based approach to hyperparameter optimization*, *Journal of Machine Learning Research* **18** (2018) 1.
- [23] C.N. Coelho, Jr et al., *Automatic heterogeneous quantization of deep neural networks for low-latency inference on the edge for particle detectors*, *Nat. Mach. Intell.* **3** (2021) 675.
- [24] AMD, *Vitis High-Level Synthesis (HLS) User Guide*, October, 2023.
- [25] AMD, *Vivado Design Suite User Guide: Design Flows Overview (UG892)*, 2024.
- [26] D.N. Gadde et al., *Effective design verification – constrained random with python and cocotb*, [2407.10312](https://doi.org/10.1016/j.procs.2017.10.312).